Overlaying 5G Radio Access Networks on Wavelength Division Multiplexed Optical Access Networks with Carrier Distribution

Xun Guan, Simon Bélanger-de Villers, Wei Shi, and Leslie A. Rusch

OSA Optics Express, (Volume 29, Issue 3) (2021)

https://doi.org/10.1364/OE.415667

Overlaying 5G Radio Access Networks on Wavelength Division Multiplexed Optical Access Networks with Carrier Distribution

Xun Guan,[1] Simon Bélanger-de Villers,[1] Wei Shi,[1] and Leslie A. Rusch[1,*]

[1] *Department of Electrical and Computer Engineering, Centre for Optics, Photonics and Lasers, Université Laval, Quebec, QC G1V 0A6, Canada*
[*] *leslie.rusch@gel.ulaval.ca*

Abstract: As 5G communication matures, the requirement for advanced radio access networks (RAN) drives the evolution of optical access networks to support these needs. Basic RAN functions, mobile front-haul to the backbone and interconnected front-end remote radio units, must support and enable data rate surges, low-latency applications, RF coordination, etc. Wavelength division multiplexed optical access networks (WDM-OANs) provide sufficient network capacity to support the addition of RAN services, especially in unused portions of WDM. We propose and demonstrate a method for RAN overlay in WDM-OANs that employ distributed carriers. In such systems, the carrier is modulated at the central office for direct-detected downstream digital data services; later the same carrier is remodulated for the uplink. We propose the use of silicon photonics to intercept the downstream and add 5G signals. We examine the distributed-carrier power budget issues in this overlay scenario. The carrier power must be harvested for direct detection of both digital and RoF services, and yet hold in reserve sufficient power for the uplink remodulation of all services. We concentrate on the silicon photonics subsystem at the remote node to add RoF signals. We demonstrate the overlay with a fabricated chip, and study strategic allocations of carrier power at the optical network units housing the radio units to support the overlay. After the successful drop and reception of both conventional WDM-OAN and the newly overlaid RoF signals, we demonstrate sufficient carrier power margin for the upstream remodulation.

1. Introduction

Not only does 5G emergence spur great progress in wireless communication, it also accelerates the revolution of optical communication networks enabling 5G. Optical networks play a pivotal role in connecting radio heads to one another, as well as to the backbone network. With soaring bandwidth needs and growing requirements for massive simultaneous connections, optical access networks must target throughput of 10 Gb/s to 50 Gb/s; later phases of 5G rollout would push this to 86 Gb/s [1]. Wavelength division multiplexing optical access networks (WDM-OAN) are promising candidates to transport 5G services in the optical domain [2], with multiple wavelengths to improve capacity.

This bandwidth upgrade must be accomplished with a firm eye on keeping system cost down. Carrier distribution and reuse avoids placing tunable laser diodes at each network termination. Various carrier reuse schemes have been studied using reflective semiconductor optical amplifiers (RSOA) [3], different modulation formats at downlink and uplink [4], and injection locking [5].

Distributed carriers in multiple WDM bands for colorless upstream were demonstrated in [6], with a periodic bandpass filter to suppress the downstream modulation at the optical network unit (ONU). In [7], a novel carrier reuse method was reported, in which only a portion of the downstream carrier was dropped for the downstream reception, with the residual carrier

remodulated for the upstream. A silicon microring resonator (MRR) filter was able to tune the amount of power split between the dropped carrier (downlink) and the residual carrier (uplink). The remodulation was performed with a silicon microring modulator (MRM).

In [8] we proposed to overlay 5G services via silicon photonics subsystems deployed at a smart edge. We overlaid 5G services onto the carrier at the remote node without interfering with the broadband services. This overlay was part of updating the remote node to a 5G smart edge to accommodate low-latency solutions for many new services, such as coordinated multi-point (CoMP) and multiple access edge computing (MEC). The overlay at close physical proximity to the network of remote radio units was accomplished with good spectral efficiency by the use of analog radio-over-fiber (analog RoF, aRoF) technology [9]. Demonstrations in [7, 8] exploited silicon photonics (SiP), showing the potential of this low-cost integrated technology in OAN. Carrier distribution was assumed for the convergence of next generation OAN and optical wireless. The upstream signal remodulation included digital services, and the RoF subchannel for latency-sensitive 5G local services at the remote node.

In [8], many challenges in generating subcarriers with an MRM were addressed, in particular frequency drift of the MRM. In this paper we examine the use of subcarrier generation in the RF domain. The overlaid signals are analog RoF at a radio frequency of 14 GHz. We use a newly designed and fabricated MRM bus that includes monitoring photodiodes. We demonstrate the excellent stabilization achievable with RF generation of subcarriers and monitoring photodiodes.

Besides addressing subcarrier generation with the distributed carrier, we also systematically examine the optimal allocation of carrier power in the distributed carrier network. The carrier power must be split across the broadband and the overlaid signals for detection at the ONU. In [7] a single carrier allocation was demonstrated using MRMs. In this work a waveshaper mimics those MRMs and we sweep power allocations. We quantify the disparate performance of each signal type and assess the sensitivity of performance to the carrier-to-signal ratios. In this paper, unlike [8], we have simultaneous reception of WDM bands rather than round robin measurements.

The rest of the paper is organized as follows. Section 2 introduces the principle of operation, including the system architecture, the overlay at a smart edge, and the carrier allocation at ONU. Section 3 describes the fabricated chip for the remote node, along with the characterization for the proposed RoF overlay. Section 4 presents the experimental setup for the transmission study, with comprehensive experiments on the partial carrier power drop for the reception of the downstream signals and the reserved power for the upstream remodulation. The simultaneous transmission of two WDM bands are also demonstrated in this section. Section 5 concludes the paper.

2. Principle of operation

2.1. System architecture

Fig. 1 depicts the system model of a WDM-OAN that supports radio access network (RAN) in 5G, following a passive optical network (PON) architecture with a tree topology. An example WDM system with three wavelengths is shown. Two fibers connect three functional units of a 5G RAN. The central units (CU) of a RAN are located at the optical line terminals (OLT) and linked by the feeder fiber to the remote node (RN) housing the distributed units (DU). The distribution fiber connects the DU to the radio units (RU) located at the ONUs. Given the hybrid nature (RAN over PON) we adopt the notation CU/OLT, DU/RN and RU/ONU. Conventional RAN traffic is supported by DU/RN that houses an arrayed waveguide grating (AWG) to distribute one wavelength per antenna tower. We address systems where all lasers sources are housed at the CU/OLT and the distributed carriers are used for both downlink direct detection, and uplink remodulation.

We propose introducing a smart edge capability at the RU/ONU to support latency-sensitive 5G services with two new functional units: a coordinated multipoint (CoMP) controller, and a

multi-access edge computing (MEC) server. The CoMP controller coordinates multiple cells at different RN/ONUs to suppress interference and increase network capacity. For example, the radio unit at ONU1 and ONU2 in Fig. 1, as inter-cell interference significantly increases for 5G dense cell deployments. Successful CoMP largely relies on the collection of heavy overhead, low latency channel state information [10, 11].

The MEC server offloads the latency-sensitive computing tasks from the cloud computing centers. This is important for many 5G new services which requires high computing power, but are vulnerable to latency. Examples include tactile network, augmented reality, intelligent healthcare, smart transportation, and so on. The relocation of the CoMP controller and MEC server from CU/OLT to RU/ONU could save a round-trip-time of 200 us from the physical transmission over a 20 km fiber between CU/OLT and RU/ONU. Network studies has proven the reduction of latency with fiber-based connections. Even where wireless connections exist between MEC servers and UE (for example, the MEC server at ONU3 and the UE associated with ONU1 and ONU2), round-trip time (RTT) is saved with a MEC supported by fiber based interconnection [12].

To support statistical multiplexing of smart edge resources and the granularity of demand for latency-sensitive services, we propose the overlay approach illustrated in Fig. 1. The dotted lines indicate that spectrally efficient and narrowband analog radio over fiber signals will be overlaid on the conventional RAN traffic. These signals are added and dropped at the RU/ONU without impact to conventional traffic.

Conventional RAN traffic travels between the CU/OLT and the antenna tower RU/ONUs in the form of digital radio-over-fiber (dRoF); today dRoF uses the common public radio interface (CPRI) [13] or the enhanced CPRI (eCPRI) [14]. We propose to overlay analog RoF signaling for the 5G traffic applications that demand low latency. The digital RoF signal will not be the OOK (on-off keying) of today's CPRI/eCPRI, but a higher throughput, non-baseband approach compatible with aRoF overlay. We propose subsystems to play the crucial role of overlaying latency-sensitive analog RoF 5G traffic while allowing conventional RAN traffic (i.e., digital RoF) to pass through. The subsystems are compatible with WDM to meet the future need of high throughput networks. Our solution is wavelength-selective to deliver the 5G services to the targeted subset of RU/ONUs with low latency requirements. The solution is also colorless, as it avoid the cost by extra lasers at the smart edge DU/RN, by exploiting the distributed carrier used for the conventional RAN signals.

2.2. Overlay at smart edge with distributed carrier

To satisfy the aforementioned requirements, the modulation of 5G signals initiated by CoMP and MEC can be realized with photonic integrated circuits (PIC) based on silicon photonics (SiP), or

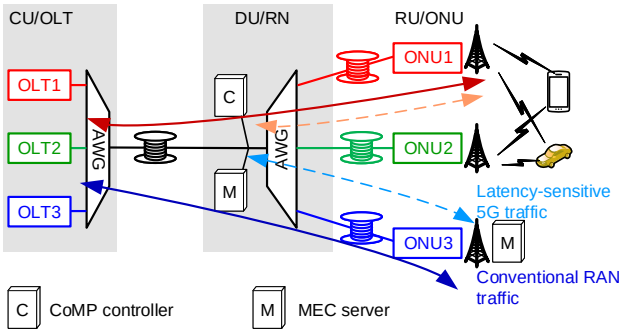

Fig. 1. System model of 5G WDM-OAN with low-latency support overlaid.

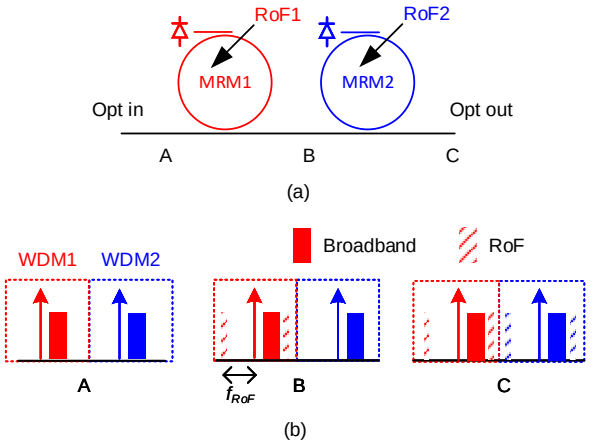

Fig. 2. RoF services overlay at the smart edge: (a) SiP MRM to overlay in different WDM bands; and (b) spectra of two-band WDM overlay.

more specifically, microring modulators (MRM), as depicted in Fig.2. An MRM is a wavelength selective modulator, whose working frequency can be tuned thermally. Wavelengths outside the MRM working range will pass through without interference and loss. As a bonus, all WDM bands can be modulated along the same bus waveguide (the multiple cascaded MRMs) without requiring optical filters. Each MRM in the cascade has the same layout; working frequencies are shifted by thermal heaters to the desired channel.

In the proposed system, the optical input (opt-in) is the WDM optical signal from the CU/OLT. Each WDM band contains a broadband signal for conventional RAN, with a distributed carrier. Because of the wavelength selectivity of the MRM, it modulates the optical carrier with the RoF signal (for CoMP and MEC) and leaves the broadband signal untouched. The input signal passes sequentially through each MRM (tuned to a WDM band), and is RoF modulated or not, depending on the requests of CoMP and MEC of each WDM band and RU/ONU. Afterwards, the arrayed waveguide gratings (AWG) routes the wavelength to the appropriate RU/ONU, as depicted in Fig. 1.

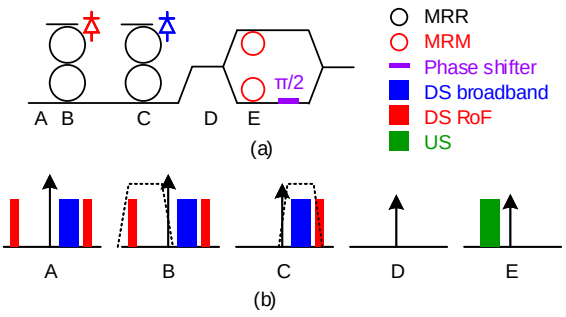

Fig. 3. Separate drops of dRoF and aRoF as well as upstream remodulation at the RU/ONU, with proposed embodiment in [7]. Dashed trapezoids depict MRR drop filter profile. MRR: microring resonator; MRM: microring modulator; DS: downstream; US: upstream.

2.3. *Partial carrier drop, downstream reception and upstream modulation at RU/ONU*

Each drop fiber transmits one WDM band to the target RU/ONU. The band contains a carrier, a broadband dRoF signal and a narrowband aRoF signal. At the RU/ONU, in [7] an SiP subsystem was proposed that would support this overlay. The RU/ONU is designed to drop both signals, and remodulate the upstream signal with the residual carrier after partial carrier drop, as seen in Fig. 3.

The RU/ONU can control the amount of carrier power dropped with microring resonator filters (MRRs). The drop port for each signal type can selectively tune the slope or transition of the filter response to only partially strip carrier power. In other words, the carrier power can be selectively allocated to demodulation of each downstream signal type, and to remodulation in the uplink. In Fig. 3, two second-order cascaded MRR filters [7, 15] are used to drop the RoF signal and broadband signal, respectively. The MRR filters have a designated transition between pass-band and stop-band. In this way, the first fully drops the RoF signal, but only strips a portion of the carrier sufficient for RoF detection. A similar second filter drops the broadband signal with another portion of the carrier power. The dropped optical signals are direct detected by Germanium silicon photodetectors integrated with the silicon subsystem.

After being stripped twice, the residual carrier reaches an MRM modulator (two branches for IQ modulation) for the remodulation of upstream data. To avoid Rayleigh back scattering (RBS), an MRM IQ modulator [16] could be used to modulate only on the single side-band [17] that is different from the downstream. The uplink signal, combined aRoF and dRoF, is then launched into the drop fiber from the RU/ONU. At the smart edge similar SiP subsystems strip off the latency-sensitive signals, leaving the dRoF untouched for continued transmission to the CU/OLT.

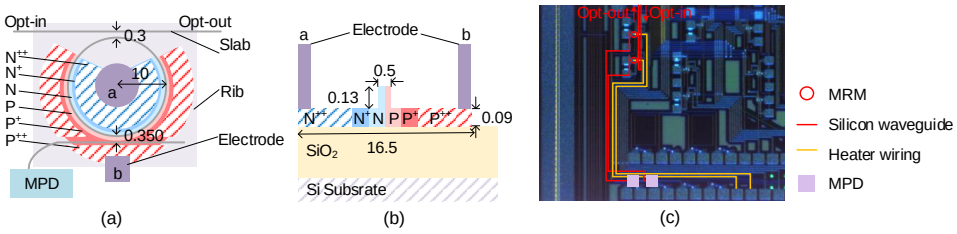

Fig. 4. Chip design layout: (a) top view, (b) side view, and (c) photo of fabricated chip

3. Smart edge chip fabrication and MRM characterization

A chip of cascaded MRMs was fabricated at AMF, Singapore, with the layout shown in Fig. 4(a) and (b) . In each MRM two straight waveguides are coupled to the ring resonator, forming an add-drop structure; an on-chip heater covering 90% of the circumference is not shown in the layout. A germanium on-chip monitor photodiode (MPD) is connected to the drop port, for the purpose of monitoring and controlling the working point of MRM via the drop-port power. A photo of the fabricated chip is shown in Fig. 4(c) with radio-frequency (RF) probes loaded for modulation; the MPD and on-chip heaters were connected via wire-bonding. The quality factor (Q-factor) of the MRM was measured to be about 15,000.

Fig. 5(a) shows the spectra of MRM transmission under different reverse bias voltages, with the input power of the scanning laser at 0 dBm. The reverse bias red-shifted the MRM resonance by about 2 GHz/V. Throughout the rest of the paper, the reverse-bias voltages of both MRM were kept at -4 V. The blue-side of the MRM transmission was used for modulation, i.e., the laser frequency was greater than the MRM resonance frequency. In Fig. 5(b) we zoom in on the -4 V reverse bias results in the boxed region in Fig. 5(a) around the blue side resonance. The x-axis is the frequency difference, f_d, between the laser and the resonance.

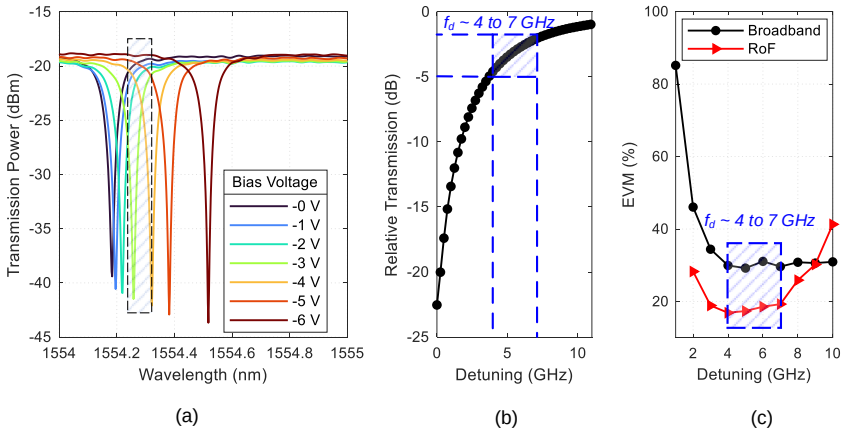

Fig. 5. (a) Measured power transmission spectra in the vicinity of MRM resonance, under different reverse bias voltages; (b) Transmission of an MRM with detuning frequency, corresponding the boxed region of (a); (c) EVM of broandband and RoF under different detuning frequencies.

In practice, the selection of f_d is a compromise of modulation depth and bandwidth. As elaborated in [18], increasing f_d boosts the MRM bandwidth, but sacrifices its optical modulation amplitude (OMA). For our application of RoF overlay, the detuning frequency also affects the amount of carrier power passed to the through-port. The choice of f_d therefore also affects the reception of both RoF and broadband signals: a larger f_d passes more carrier power benefiting broadband signal reception. However, the increase of f_d reduced the OMA of MRM, thus deteriorating the performance of RoF. In contrast, when f_d is too small, for example, at 0 GHz, the optical carrier would be too weak for broadband signal reception; and the RoF signal would be clipped by the non-monotonic response around the MRM resonance.

In the characterization of MRM, as well as in the transmission experiments to follow, the broadband signal was set to be single side-band quadrature phase shift keying orthogonal frequency division multiplexing (SSB-QPSK-OFDM) ranging from 4 GHz to 12 GHz. The RoF signal was an 1 Gbaud QPSK-OFDM at an radio frequency of 14 GHz. Note that the bandwidth and RF frequency selection was limited not by the SiP subsystem, but rather by the digital to analog converter (DAC); it was sufficient for a proof-of-concept study.

We conducted a series of experiments to find the optimal detuning frequency. The variation of error vector magnitude (EVM) of both broadband signal and RoF, as a function of f_d, is shown in Fig. 5(c). Taking into consideration the performance of both signals, an appropriate detuning frequency range is as wide as 3 GHz to 7 GHz.

The insertion loss of an MRM originates from two factors. The first factor is related the operating point. For our chosen detuning range, a -2 dB to -5 dB loss is introduced. This is the inherent loss of modulation, similar to that of other modulators, such as a Mach-Zehnder modulator (MZM). This loss does not accumulate in a bus of MRMs, thanks to their wavelength selectivity. Hence, it does not limit the channel number.

The other factor is the excess loss, or the propagation loss. This loss would accumulate on an MRM bus. One contribution is the waveguide transmission; silicon photonics generally have attenuation of 2 dB/cm. Because of the MRM small footprint (tens ofμm), the waveguide propagation loss is very low. A second contribution to propagation loss is filtering from the MRM for the neighbouring WDM channel. As can be seen in Fig. 5(b), due to the MRM's high Q-value and fast roll-off, this loss is also negligible. The overall propagation loss should be lower

than a dB without further optimization, even when supporting tens of channels.

4. Transmission experiments

4.1. Experimental setup

The experimental setup to study the transmission in OAN is depicted in Fig. 6. Two Cobrite external cavity lasers, running at 1553.33 nm and 1554.13 nm with a 100 GHz frequency spacing, were split using a 50/50 optical coupler. One copy of the carriers was modulated by an I/Q modulator (SHF). The broadband signal was generated offline and passed to a digital-to-analog converter (DAC, Fujitsu Leia 64 GSa/s, 13 GHz bandwidth). The other copy of the carriers was rejoined to the modulated optical signal as the distributed carrier. The fast-Fourier transform (FFT) size of the OFDM broadband signal was 2048, while 256 subcarriers were used, to range from 4 GHz to 12 GHz. A cyclic prefix (CP) of 10 sample was inserted. Each OFDM packet contains 120 symbols, of which 10 were used as the training sequence. Four subcarriers out of 256 were used to correct the common phase error (CPE). The final net bit rate of the broadband signal was 14.3 Gb/s.

After travelling through a 20 km trunk fiber, the optical signal was amplified with an erbium doped fiber amplifier (EDFA, INO FAD series). We adjusted the polarization before entering the chip since we used grating couplers (GC) that work only for the transverse-electric (TE) mode. Deployed systems could use polarization insensitive technologies, like edge coupling [19]. The in-and-out loss of the chip was 19 dB, see Fig. 5(a), of which more than 17 dB was introduced by the coupling loss of GC due to the immature coupling technology in lab experiments. With advanced optical packaging methods, the loss could be reduced to 1.6 dB [20]. EDFA1 boosted the optical signal power by 8 dB.

On chip, the optical signal sequentially passed two MRM and was modulated by the RoF signals (DAC, Fujitsu Leia 64 GSa/s, 13 GHz bandwidth). The MRM was direct current bias loaded with a bias-T. The aRoF signal was a 2048-FFT QPSK-OFDM signal. The subcarriers were selected to form RoF signals centering at 14 GHz, with 32 subcarrier occupying an 1 GHz bandwidth. Similarly by deducting 10-sample CP, 10/120 training sequence and 4 subcarriers for CPE correction, the final bit rate of RoF signal was 1.6 Gb/s. The on-chip MPD detected the drop-port power and captured with a data acquisition card (DAQ, National Instrument USB6009). The monitoring signals from both MPD were fed to a closed loop proportional integral derivative

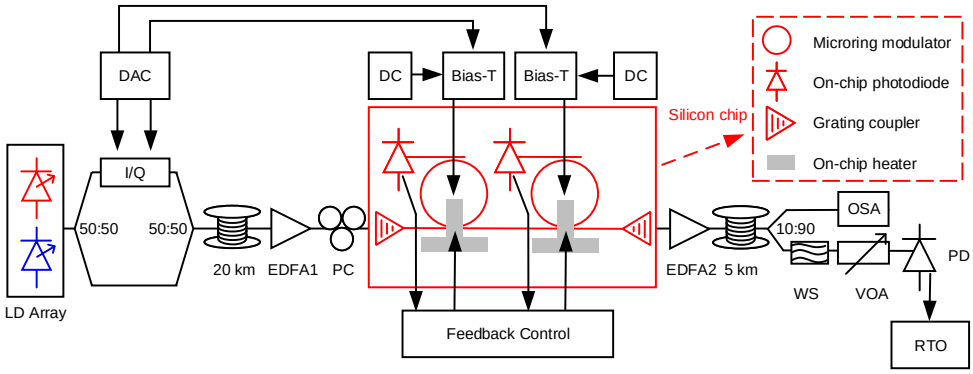

Fig. 6. Experimental setup. LD: laser doide, DAC: digital-to-analog converter, DC: direct current source, EDFA: erbium-doped fiber amplifier, PC: polarization controller WS: waveshaper, VOA: variable optical attenuator, OSA: optical spectrum analyzer, PD: photodiode, RTO: real-time oscilloscope.

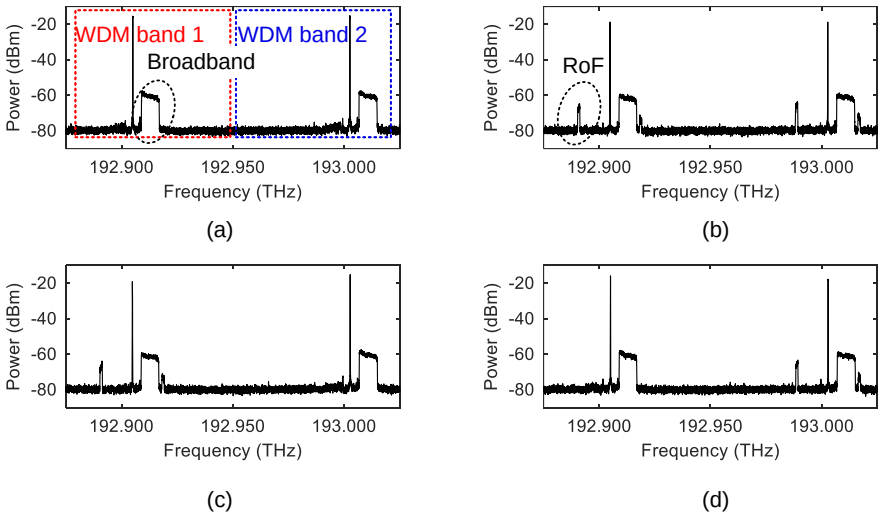

Fig. 7. Spectra of 5G-OAN; (a) No RoF overlay in either WDM; (b) RoF overlay in both WDM; (c) RoF overlay in WDM1 only; (d) RoF overlay in WDM2 only.

(PID) controller, while the control signal adjusted the driving signals on on-chip heaters to stabilize the MRM. The RoF overlay on either WDM band or both WDM could be achieved by adjusting the MRM working frequencies. Fig. 7 shows the measured optical spectra in different cases of aRoF overlay. The asymmetry in the two sidebands of aRoF were caused by the inherent transient time dynamics of MRM, as explained in [21]. However, it did not affect the detection of aRoF, as optical filters at the RU/ONU filtered out only one sideband.

After the chip, the signal was boosted by another EDFA2 (14 dB gain), passed though a reel of 5 km drop fiber and reached the RU/ONU side. The two EDFA before and after the chip, with a total gain of 22 dB, compensated the 20 dB GC loss. Note that with advanced packaging to reduce the loss, both EDFAs could be eliminated. After another transmission over 5 km in single mode fiber, 10% of received power was split to monitor the optical spectra with a high-resolution optical spectrum analyzer (OSA, Apex technologies AP2043), while the other 90% was used for reception. A waveshaper (Finisar 4000S) was used to emulate the functionality of RU/ONU MRRs, by mimicking the drop filter profile and transition. A variable optical attenuator (VOA) adjusted the received power before entering PD (Agilent 11982A). The signal was captured with a real-time oscilloscope (RTO, Agilent Infiniium 90000, 80 GSa/s) for offline processing.

4.2. Carrier partial drop ratio and power budget

To emulate the carrier partial drop reception of both broadband and RoF signals, as well as the remaining carrier budget for upstream remodulation, the waveshaper was set as a Lorentzian roll-off filter as in the case of MRR [22]. The bandwidth of the filter was 30 GHz, while the transition rolled off 3 dB at 5 GHz one-sided. By keeping the shape but varying the central frequency of the optical filter, the dropped power of the carrier was varied by different transmission ratio at the edge of the filter. A graphical depiction of the drop filter and carrier drop ratio is shown in Fig. 8.

Throughout the experiments, we report the carrier drop ratio, R. The waveshaper mimics the drop port, so the output carrier power is the power used a single detection. The ratio in dB is given by

$$R = 10\log(P_{in}/P_{out}), \tag{1}$$

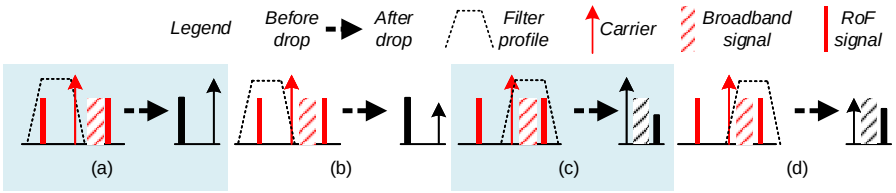

Fig. 8. RoF signal reception with (a) higher carrier power therefore lower carrier drop ratio, (b) higher drop ratio; Broadband signal reception with (c) lower drop ratio, (d) higher drop ratio. The carrier power, or drop ratio, was varied by fixing the filter bandwidth but changing its central frequency.

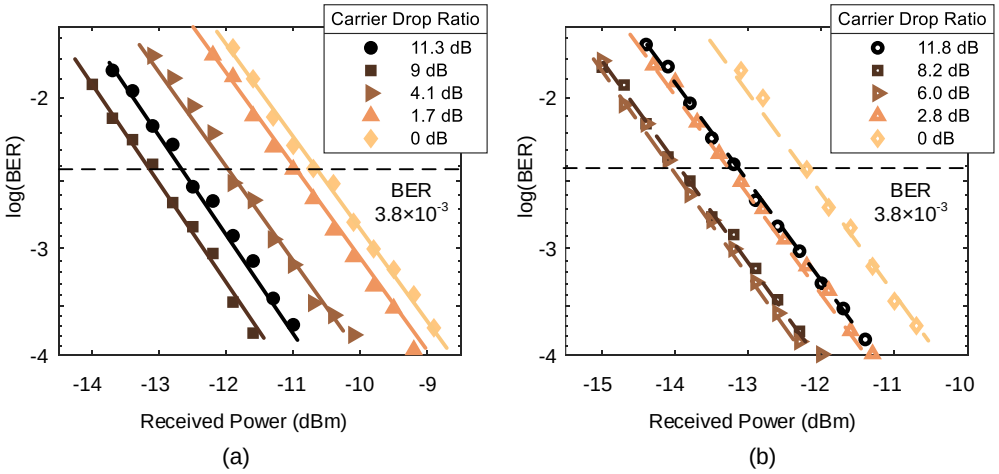

Fig. 9. (a) BER of RoF signal with regard to received power under different carrier drop ratio ratios; (b) BER of broadband signal with regard to received power under different carrier drop ratio ratios

where P_{in} is the input carrier power to the waveshaper, and P_{out} is the output carrier power. As we work in a system with a distributed carrier, carrier power must be husbanded for many requirements - detection of RoF, detection of broadband transmissions, and retransmission of both RoF and broadband signals. For example, a carrier drop ratio of 0 dB indicates $P_{out} = P_{in}$, i.e., all carrier power is used for one reception. A carrier drop ratio of 6 dB drops 1/4 of the carrier power, preserving 3/4 of the carrier for other reception or retransmission.

For the RoF signal, the bit-error-rate versus received power, under different carrier drop ratio, is depicted in Fig. 9(a). A smaller dB number in carrier drop ratio means the carrier was attenuated less by the filter, and more carrier power was with the signal reception; it corresponds to the case of Fig. 8(a). A larger dB number, in contrast, matches with Fig. Fig. 8(b). From Fig. 9(a), it could be found that when carrier drop ratio increased from 0 dB (i.e. the whole carrier was with the signal reception), the received power request for a given BER level decreased. This was because that there was excessive carrier power for the RoF signal. While the carrier was partially stripped away, the carrier-to-signal ratio decreased, and with the same received power at PD, the RoF signal was stronger, facilitating the reception. However, when the carrier was dropped more than 9 dB, the carrier power was no longer redundant for RoF reception; and the further increase of carrier drop ratio would in turn impair the RoF reception, and decrease the BER with the same received power. A similar trend could be observed from the reception of broadband signal, as in

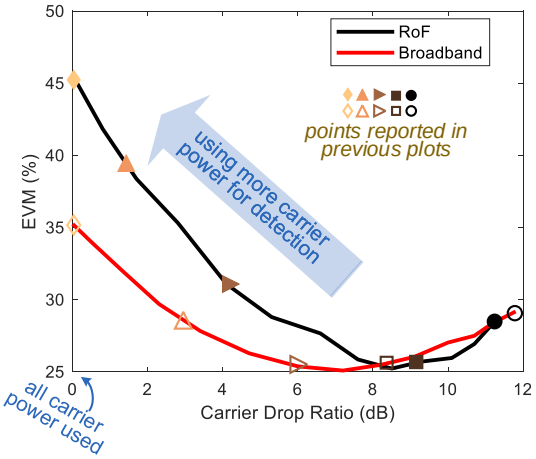

Fig. 10. EVM of RoF and broadband signals under different carrier drop ratio

Fig. 9(b), only that the turning point appeared to be between 6.0 dB and 8.2 dB.

To find the BER performance under different carrier drop ratios, we varied the carrier drop ratio, but kept the received power constant for RoF (-11 dBm) and broadband (-12 dBm) signals. Fig. 10 shows the error vector magnitude (EVM) versus carrier drop ratio for the two signals. We conclude that to conserve power with minimal impact on performance, the RoF signal could be dropped at a drop ratio of 8.5 dB, while the broadband signal performed best at around 7.2 dB. The slight difference in this power ratio should be attributed to the RoF and broadband signals having different modulation depth and different carrier to signal ratio after modulation.

4.3. WDM transmission

We measured bit error rate (BER) for the simultaneous transmission of both WDM bands, including the two broadband and two RoF signals. Results are presented in Fig. 11. The carrier drop ratios were set around the optimal values for both broadband and RoF signals in both WDM bands: at 7.6 dB for RoF and 7.2 dB for broadband. Taking into account both carrier drop ratios, the dropped carrier for the reception of the two downstream signals was only 36% of the available carrier power. This left ample power margin for upstream remodulation. All four signals could achieve BER lower than 3.8×10^{-3}, the hard-decision forward error correction (HD-FEC).

The required received power for the HD-FEC threshold in RoF was about 1 dB higher than in broadband for two reasons. Firstly, the dropped carrier power was (7.2 dB for broadband reception versus 7.6 dB) for RoF reception. Secondly, at the reception of RoF, the broadband signal was not totally filtered out. The residual broadband signal also contributed slightly to the received power, thus artificially increasing its value. In comparison, RoF was lower in bandwidth and higher in frequency, thus tended to be filtered more with the drop filter when receiving broadband signal.

4.4. MRM stabilization

Although benefiting from wavelength selectivity, the temperature dependence of MRM makes its application challenging. The working wavelength could drift if not well controlled. There have been several studies on the tracking and control algorithms of MRM stabilization [23–25]. In this work, an on-chip MPD was added to the drop-port of MRM to monitor the dropped optical power during modulation. The monitor signal was captured with an DAQ

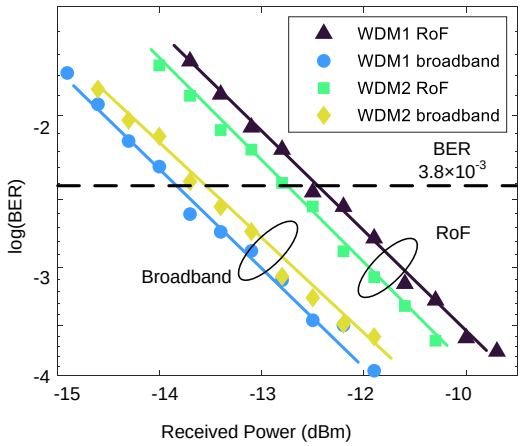

Fig. 11. BER of broadband and 5G RoF signals in two WDM bands

card (National Instrument USB6009), for feedback control of the MRM thermal condition via a proportional–integral–derivative (PID controller). The stabilization performance was experimentally studied by introducing a step change to the heater voltage to perturb the MRM working frequency. The BER of the RoF signal with the PID turned on and off are shown in Fig. 12. While stabilization was activated, the BER returned to below the HD-FEC threshold. This completely counteracted the loss of performance without the stabilization. This experiment demonstrates the effectiveness of the MRM stabilizer with simple on chip monitoring of a drop port.

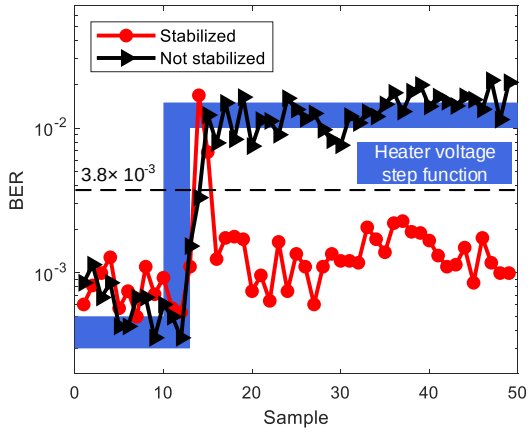

Fig. 12. The demodulated BER of 5G RoF without and with stabilization.

5. Conclusion

In this paper we address 5G WDM-OANs with carrier distribution from CU/OLT to DU/RN and RU/ONU. The RU/ONU is transformed into a smart edge with the functionality of CoMP and MEC. The smart edge accesses latency-sensitive transmission by exploiting RoF signals overlaid in the WDM bands. A sample chip for the smart edge subsystem was fabricated and

experimentally validated, with broadband and overlaid RoF signals detectable below HD-FEC. The design also includes a stabilization unit that employs an on-chip MPD to monitor the drop power of MRM. It resolves the drift of MRM resonance and working frequency. At the RU/ONU, the distributed carrier could be partially dropped for both the broadband signal and RoF signal, while leaving sufficient residual carrier for upstream remodulation. The carrier allocation at RU/ONU is experimentally studied; after dropping enough power for the reception of both broadband and RoF, it leaves more than 60% of the carrier power for the upstream remodulation.

Disclosures

The authors declare no conflicts of interest.

References

1. J. S. Wey and J. Zhang, "Passive optical networks for 5G transport: technology and standards," J. Light. Technol. **37**, 2830–2837 (2018).
2. E. Wong, E. Grigoreva, L. Wosinska, and C. M. Machuca, "Enhancing the survivability and power savings of 5G transport networks based on DWDM rings," J. Opt. Commun. Netw. **9**, D74–D85 (2017).
3. W.-J. Jiang, C.-T. Lin, P.-T. Shih, J. J. Chen, P.-C. Peng, and S. Chi, "A full duplex radio-over-fiber link with multi-level OFDM signal via a single-electrode MZM and wavelength reuse with a RSOA," Opt. express **18**, 2710–2718 (2010).
4. H.-C. Ji, H. Kim, and Y. C. Chung, "Full-duplex radio-over-fiber system using phase-modulated downlink and intensity-modulated uplink," IEEE Photonics Technol. Lett. **21**, 9–11 (2008).
5. Z. Xu, Y. J. Wen, W.-D. Zhong, T. H. Cheng, X. Cheng, Y. Wang, and Y.-K. Yeo, "10 Gb/s WDM-PON based on FP-LDs injection locked by downlink optical carrier," Opt. communications **281**, 5213–5217 (2008).
6. C. Lei, H. Chen, M. Chen, and S. Xie, "16$\times$ 10Gb/s symmetric WDM-FOFDM-PON realization with colorless ONUs," Opt. Express **19**, 15275–15280 (2011).
7. M. Lyu, W. Shi, and L. A. Rusch, "Silicon photonic subsystem for broadband and RoF detection while enabling carrier reuse," Opt. Express **28**, 14897–14907 (2020).
8. X. Guan, R. Dubé-Demers, W. Shi, and L. Rusch, "Heterogeneous optical access networks: Enabling low-latency 5G services with a silicon photonic smart edge," J. Light. Technol. (2020). Accepted with minor revisions.
9. G. Giannoulis, N. Argyris, N. Iliadis, G. Poulopoulos, K. Kanta, D. Apostolopoulos, and H. Avramopoulos, "Analog radio-over-fiber solutions for 5G communications in the beyond-CPRI era," in *2018 20th International Conference on Transparent Optical Networks (ICTON),* (IEEE, 2018), pp. 1–5.
10. V. Jungnickel, K. Manolakis, W. Zirwas, B. Panzner, V. Braun, M. Lossow, M. Sternad, R. Apelfröjd, and T. Svensson, "The role of small cells, coordinated multipoint, and massive MIMO in 5G," IEEE communications magazine **52**, 44–51 (2014).
11. R. Irmer, H. Droste, P. Marsch, M. Grieger, G. Fettweis, S. Brueck, H.-P. Mayer, L. Thiele, and V. Jungnickel, "Coordinated multipoint: Concepts, performance, and field trial results," IEEE Commun. Mag. **49**, 102–111 (2011).
12. J. Xue and G. Shou, "How far can optical access networks support in multi-access edge computing for low delay?" in *Optical Fiber Communication Conference,* (Optical Society of America, 2018), pp. Tu2G–4.
13. A. Ericsson *et al.*, "Common public radio interface (CPRI); interface specification v7. 0," Huawei Technol. Co. Ltd, NEC Corp. Alcatel Lucent, Nokia Networks (2015).
14. G. Kalfas, M. Agus, A. Pagano, L. A. Neto, A. Mesodiakaki, C. Vagionas, J. Vardakas, E. Datsika, C. Verikoukis, and N. Pleros, "Converged analog fiber-wireless point-to-multipoint architecture for eCPRI 5G fronthaul networks," in *2019 IEEE Global Communications Conference (GLOBECOM),* (IEEE, 2019), pp. 1–6.
15. L. Zhang, H. Zhao, H. Wang, S. Shao, W. Tian, J. Ding, X. Fu, and L. Yang, "Cascading second-order microring resonators for a box-like filter response," J. Light. Technol. **35**, 5347–5360 (2017).
16. P. Dong, C. Xie, L. Chen, N. K. Fontaine, and Y.-k. Chen, "Experimental demonstration of microring quadrature phase-shift keying modulators," Opt. letters **37**, 1178–1180 (2012).
17. Y. Xu, M. Lyu, L. Rusch, and W. Shi, "Silicon microring IQ modulator enabled single sideband OFDM transmission," in *Optical Fiber Communication Conference,* (Optical Society of America, 2019), pp. Th2A–28.
18. H. Yu, D. Ying, M. Pantouvaki, J. Van Campenhout, P. Absil, Y. Hao, J. Yang, and X. Jiang, "Trade-off between optical modulation amplitude and modulation bandwidth of silicon micro-ring modulators," Opt. express **22**, 15178–15189 (2014).
19. B. B. Bakir, A. V. De Gyves, R. Orobtchouk, P. Lyan, C. Porzier, A. Roman, and J.-M. Fedeli, "Low-loss ($<$1 db) and polarization-insensitive edge fiber couplers fabricated on 200-mm silicon-on-insulator wafers," IEEE Photonics Technol. Lett. **22**, 739–741 (2010).
20. N. Lindenmann, G. Balthasar, D. Hillerkuss, R. Schmogrow, M. Jordan, J. Leuthold, W. Freude, and C. Koos, "Photonic wire bonding: a novel concept for chip-scale interconnects," Opt. express **20**, 17667–17677 (2012).
21. J. Müller, F. Merget, S. S. Azadeh, J. Hauck, S. R. García, B. Shen, and J. Witzens, "Optical peaking enhancement in high-speed ring modulators," Sci. reports **4**, 6310 (2014).

22. B. E. Little, S. T. Chu, H. A. Haus, J. Foresi, and J.-P. Laine, "Microring resonator channel dropping filters," J. lightwave technology **15**, 998–1005 (1997).
23. K. Padmaraju, D. F. Logan, T. Shiraishi, J. J. Ackert, A. P. Knights, and K. Bergman, "Wavelength locking and thermally stabilizing microring resonators using dithering signals," J. Light. Technol. **32**, 505–512 (2013).
24. Z. Wang, D. Paez, A. I. Abd El-Rahman, P. Wang, L. Dow, J. C. Cartledge, and A. P. Knights, "Resonance control of a silicon micro-ring resonator modulator under high-speed operation using the intrinsic defect-mediated photocurrent," Opt. Express **25**, 24827–24836 (2017).
25. H. Jayatilleka, K. Murray, M. Á. Guillén-Torres, M. Caverley, R. Hu, N. A. Jaeger, L. Chrostowski, and S. Shekhar, "Wavelength tuning and stabilization of microring-based filters using silicon in-resonator photoconductive heaters," Opt. express **23**, 25084–25097 (2015).